Properties of vortex light fields generated by generalized spiral phase plates

Svetlana N. Khonina [1,2] Andrey V. Ustinov,[1] Valentin I. Logachev,[2] and Alexey P. Porfirev[1,2]
[1]Image Processing Systems Institute of RAS–Branch of the FSRC "Crystallography and Photonics" RAS, 151 Molodogvardeyskaya str., Samara 443001, Russia
[2]Samara National Research University, 34 Moskovskoye shosse, Samara 443086, Russia

(Received 29 January 2020; accepted 31 March 2020; published 22 April 2020)

We present a theoretical and experimental investigation of a diffractive optical element—a generalized spiral phase plate (GSPP) with a transmission function of $\exp[ig(\varphi)]$, where $g(\varphi)$ is an unambiguous function. In contrast to the conventional spiral phase plate that is widely used for the generation of ring-shaped vortex beams with an orbital angular momentum (OAM), the GSPP can be used for the generation of nonring (including spiral-shaped) laser beams with a helical wave front. Some examples of the function $g(\varphi)$ were investigated in detail, showing the features arising in these cases. The proposed GSPP demonstrates angle-dependent distortion resistance properties, whereby for different angular positions of an opaque obstacle on the surface of the element, different values of root-mean-square error are obtained. The angular harmonics spectra of the generated vortex light fields strongly depend on the growth rate of the function $g(\varphi)$. In addition, the OAM density of the generated nonring light fields is nonuniform and the total OAM also depends on the angular coordinate of the obstacle. The experimentally and numerically obtained results are in good qualitative and quantitative agreement.

DOI: 10.1103/PhysRevA.101.043829

I. INTRODUCTION

The spiral phase plate (SPP), an optical element with a complex transmission function $\mathrm{circ}(r/R)\exp(im\varphi)$, where (r, φ) are the polar coordinates, R is a radius of the element, and m is its topological charge (TC), was introduced in 1992 by Khonina *et al.* as "a phase rotor filter" [1], as well as by Higgins as "a spiral waveplate" [2]. The spiral phase plate (SPP) allows one to generate ring-shaped laser beams with a spiral wave front from incident plane wave, optical vortex (OV) beams [3]. Due to their unique structure, OVs have an orbital angular momentum (OAM) [4], which can be transferred from radiation to matter, thus, for example, causing the rotation of microspheres around its axis [5]. Moreover, OVs have applications in optical communication [6], optical microscopy [7], and laser material processing [8].

The conventional ideal SPP operates by directly imposing a spiral phase profile $\exp(im\varphi)$ onto the incident laser beam and theoretically allows one to convert almost 100% of the incident radiation into an OV beam. Presently, SPPs are the most popular element for the generation of OVs. However, conventional SPPs can be used only for the generation of ring-shaped or axisymmetric intensity distributions with a uniform OAM density. Recently, it has been shown that additional control of the structure of the generated vortex fields provides new opportunities, primarily in applications such as laser material processing [9,10] and optical manipulation [11,12]. In addition, the possibility of the generation of vortex fields with a desired structure of the intensity and phase gradient, which makes it possible to form light fields with an inhomogeneous OAM density, is important from a fundamental point of view, since it allows better investigation of the laser-matter interaction.

An unconventional SPP was introduced in 2014 [13], the spiral phase distribution of which also increased with the azimuthal angle; however, it does not change linearly, as in the case of a conventional SPP, and has a nonlinear dependence described as $2\pi m(\varphi/2\pi)^s$, where s is an arbitrary number. An OV beam formed by this element has a spiral shape with a gradient of intensity and phase. In this case, the OAM of the generated light fields is directly related to the value of m. Subsequently, the propagation of such OVs in free space and in the case of their focusing was studied, showing that the intensity distribution of the formed OV depends on the order of degree s, while the value m determines the size of the generated distribution [14]. In addition, it was shown that the generated singularity points move during propagation. The unique structure of such "power-exponent-phase" OVs determines the energy flow directed in spirals, which can undoubtedly find application in the field of laser manipulation of nano- and microscale objects.

In this study, we consider a general case of a SPP with a phase that is defined by an arbitrary smooth function $g(\varphi)$, whose derivative is also smooth, that is, a generalized SPP (GSPP), and investigate the properties of the vortex light fields generated by this element. The phase transmission function of such GSPP is defined as $\tau(\varphi) = \exp[ig(\varphi)]$. We analytically derive the equation for calculation of the normalized OAM of the generated light field and analytically show that its value equals the "total vortex strength" of the GSPP. The obtained description of the focal distribution is true for an arbitrary function $g(\varphi)$. Particular attention is paid to the formation of a spiral focal intensity distribution. For this, the function $g(\varphi)$ must have a monotonic derivative. Examples of such functions are power dependence [13], dependence in the form of a Gamma function [15], logarithmic, exponential, etc. It should be noted that the profiles of the transmission function of GSPP for spiral intensity forming are very similar. However, due to variations in the nonlinear dependence, the shape of the focal spiral can be controlled.

II. THEORETICAL INVESTIGATION

A. TC and OAM of the light fields generated by GSPPs

Let us start with the study of the physical properties of the proposed GSPP. For a GSPP, it is possible to introduce a value analogous to the TC of a conventional SPP, previously known as the "total vortex strength" (TVS) [16,17]. This value in the case of an arbitrary light field with a complex amplitude $E(r,\varphi)$ can be defined as follows [18]:

$$\hat{n} = \mathrm{TVS} = \frac{1}{2\pi}\lim_{r\to\infty}\int_0^{2\pi}\left[\frac{\partial \arg E(r,\varphi)}{\partial\varphi}\right]d\varphi = \frac{1}{2\pi}\lim_{r\to\infty}\mathrm{Im}\int_0^{2\pi}\left[\frac{1}{E(r,\varphi)}\frac{\partial E(r,\varphi)}{\partial\varphi}\right]d\varphi. \tag{1}$$

For a GSPP, $E(r,\varphi) = \exp[ig(\varphi)]$ and

$$\hat{n} = \mathrm{TVS} = \frac{g(2\pi) - g(0)}{2\pi}. \tag{2}$$

It is well known that the OAM of a light field with the complex amplitude $E(r,\varphi)$ can be defined as [19]

$$J_z = \mathrm{Im}\int_0^\infty\int_0^{2\pi}\left[E^*(r,\varphi)\frac{\partial E(r,\varphi)}{\partial\varphi}\right]r\,dr\,d\varphi. \tag{3}$$

If we substitute $E(r,\varphi) = \exp[ig(\varphi)]$ in Eq. (3), then the OAM of the light field $E(r,\varphi)$ in the case of a GSPP is

$$J_z = \mathrm{Im}\int_0^R\int_0^{2\pi}\exp[-ig(\varphi)]i\frac{\partial g(\varphi)}{\partial\varphi}\exp[ig(\varphi)]r\,dr\,d\varphi = \int_0^R r\,dr\int_0^{2\pi}\frac{\partial g(\varphi)}{\partial\varphi}d\varphi = \frac{R^2}{2}[g(2\pi) - g(0)]. \tag{4}$$

After normalization to the power of the light field:

$$W = \int_0^\infty\int_0^{2\pi}[E^*(r,\varphi)E(r,\varphi)]r\,dr\,d\varphi, \tag{5}$$

which, in this case, is equal to πR^2, so the normalized OAM can be defined as follows:

$$j_z = \frac{J_z}{W} = \frac{g(2\pi) - g(0)}{2\pi} = \hat{n}. \tag{6}$$

It is evident that the normalized OAM is equal to TVS, analogous to the case of a conventional SPP.

A special case of a GSPP is a power exponent SPP with the transmission function of $\tau(\varphi) = \exp(ia\varphi^p)$;, when $p = 1$, the power exponent SPP transforms to a conventional SPP. The case of $p = 2$ was investigated in [13]. For a power exponent SPP, it is possible to calculate the TVS and OAM explicitly as

$$\hat{n} = a(2\pi)^{p-1}. \tag{7}$$

For $p = 1$, $\hat{n} = a$ is true for a conventional SPP, even with a SPP with a fractional TC.

B. Light field distributions generated by GSPPs in the far-field region

It is well known that a conventional SPP with an integer TC generates a ring-shaped intensity distribution. The power exponent SPP with $p = 2$ generates the intensity distribution in the form of one coil of the spiral [13,14]. The proposed GSPP can generate intensity distributions that are different from spirals. Let us consider the generation of the light curve in the far-field region when illuminating a GSPP with a plane wave. One of the conventional approaches for analyzing the diffraction of laser radiation by phase diffractive optical elements is the representation of the transmission function of the element in the form of a Fourier series, that is, as a combination of conventional SPPs. In our case, it has the following form:

$$\exp[ig(\varphi)] = \sum_n c_n\exp(in\varphi), \tag{8}$$

where the coefficients c_n are calculated as follows:

$$c_n = \frac{1}{2\pi}\int_0^{2\pi}\exp[ig(\varphi)]\exp(-in\varphi)d\varphi. \tag{9}$$

In particular, this analytical approach was applied in the analysis of the diffraction of laser radiation by a conventional SPP with a fractional TC [18,20]. The series expansion allows one to calculate TVS as follows:

$$\hat{n} = \sum_n n|c_n|. \tag{10}$$

Using the same expansion, we can get an expression for the normalized OAM of the light field as follows:

$$j_z = \sum_n n|c_n|^2 \Big/ \sum_n |c_n|^2. \tag{11}$$

These equations are especially useful in cases where Eqs. (2) and (4) cannot be applied, for example, when processing experimental data and there is no analytical expression for the field amplitude. However, the representation of Eq. (8) is not convenient for describing the intensity distribution in the far-field region. In many cases, the analytical calculation of the coefficients in Eq. (9) is impossible, even for fairly simple functions like $\exp(ia\varphi^p)$. The decomposition in Eq. (8) corresponds to a combination of ring-shaped distributions with different complex coefficients, from which it is difficult to obtain the structure of the total intensity. For example, for a conventional SPP with a fractional TC equal to 0.5, a crescent-shaped image is formed, but obtaining such a result from Eqs. (8) and (9) is not obvious. Therefore, a different approach was used considering the diffraction of laser radiation by a GSPP with the transmission function of $\exp[ig(\varphi)]$ in the focal plane of a lens using the Fourier transform in polar coordinates:

$$E(\rho,\theta) = \frac{k}{f}\iint_\Omega \exp[ig(\varphi)]\exp\left[-i\frac{k}{f}r\rho\cos(\varphi-\theta)\right]r\,dr\,d\varphi. \tag{12}$$

The exact calculation of the field defined by Eq. (12) is difficult even for a power exponent SPP, but an approximate description is relatively easy. A conventional SPP with an integer TC m generates a radially symmetric intensity distribution:

$$E(\rho,\theta)=\frac{k}{f}\iint_{\Omega}\exp\left(im\varphi\right)\exp\left(-i\frac{k}{f}r\rho\,\cos\left(\varphi-\theta\right)\right)r\,dr\,d\varphi$$
$$=\frac{2\pi k}{f}i^{m}\exp\left(im\theta\right)\int_{0}^{R}J_{m}\left(\frac{k}{f}r\rho\right)r\,dr. \tag{13}$$

The analytically calculated integral in Eq. (13) is known [21], but it is expressed in general terms through a hypergeometric function, which is not convenient for analysis. For specific values of m, explicit expressions can be obtained, which have a finite number of terms, among which the main term is proportional to $J_{m+1}(\frac{k\rho R}{f})/(\frac{k\rho R}{f})$. If the entrance pupil is a narrow ring, then the integral in Eq. (13) is calculated trivially, and the intensity is proportional to $J_m^2(\frac{k\rho R}{f})$. It can be shown that the position of the maximum in both cases will be approximately the same and equal to

$$\rho_{\max}=\gamma'_{1,m}\frac{f}{kR}, \tag{14}$$

where $\gamma'_{1,m}$ is the first zero value of the derivative of the mth-order Bessel function (for which the mth-order Bessel function has a first maximum). Furthermore, when analyzing the distribution in the focal plane, Eq. (14) was used as the values are easy to obtain using tables of special functions.

Then, the following approach can be applied to the description of the diffraction of laser radiation by a GSPP. The plate region is divided into angular sectors so that for the nth sector defined by the range of angles $\varphi_n \leqslant \varphi \leqslant \varphi_{n+1}$, the “local” charge changes from n to $n+1$. Mathematically, this means that the following representation is used:

$$\exp[ig(\varphi)]=\sum_{n}\mathrm{rect}\left(\frac{\varphi-(\varphi_n+\varphi_{n+1})/2}{\varphi_{n+1}-\varphi_n}\right)\exp(ia_n\varphi),$$
$$n\leqslant a_n\leqslant n+1. \tag{15}$$

The sum in Eq. (15) can be either finite or infinite, with the local charge meaning

$$n_c=\frac{dg(\varphi)}{d\varphi}. \tag{16}$$

Note that when the local TC is integrated in Eq. (16) over the entire range of angles, the TVC obtained is defined by Eq. (3). From the above considerations, the range of angles of each sector is defined as follows:

$$n\leqslant\frac{dg(\varphi)}{d\varphi}\leqslant n+1. \tag{17}$$

Thus, within a given sector, the light curve of maximum intensity lies between two envelope circles (see Fig. 1). The inner circle has a radius of r_n and corresponds to the light ring generated in the case of the SPP with the phase of $\exp(in\varphi)$, whereas the outer circle has a radius r_{n+1} and corresponds to the light ring generated in the case of the SPP with the phase of $\exp[i(n+1)\varphi]$. The generated light curve passes through the nodal points, where the same circle from the outer envelope turns into the inner circle. The last angular sector is incomplete; therefore, the external envelope can be quite far from the curve, as always occurs at the beginning of the sector. However, the endpoints do not break off abruptly as in Fig. 1; the spiral continues a little beyond their limits due to diffraction.

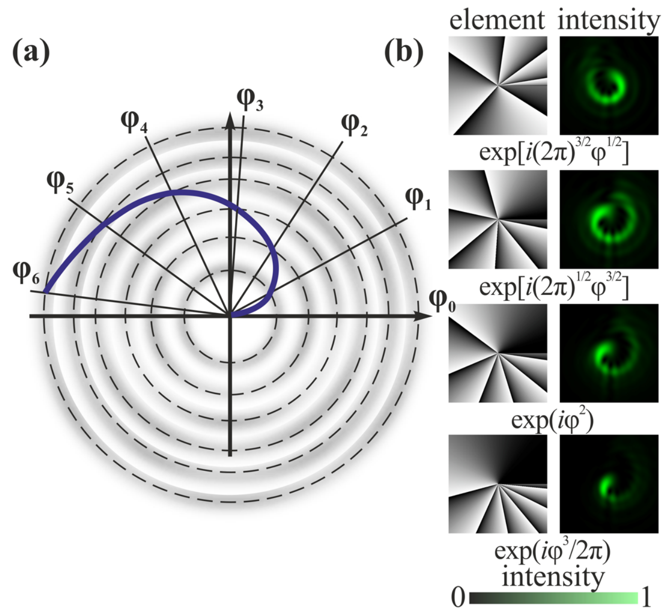

FIG. 1. Theoretical analysis of the nonring light fields generated by GSPPs with the transmission function of $\exp[ig(\varphi)]$. (a) Calculated envelopes and an approximate view of the generated light curve for the first six angular sectors in the case of $g(\varphi)=\varphi^2$ [$g'(\varphi)$ yields sectors with the same angular size]. (b) Examples of light fields generated by GSPPs with various functions $g(\varphi)$.

From the above reasoning, it follows that there is not necessarily a spiral coil of familiar form with a constantly growing or decreasing radius vector. Since the radius of the envelopes depends on the derivative $g'(\varphi)$, this form (a coil of the spiral) occurs when the derivative is a monotonic function. Otherwise, the shape is distorted, and when the equality $g'(2\pi)=g'(0)$ is fulfilled, the curve will generally be closed. To illustrate, several examples of power exponent SPPs with the transmission function of $\tau(\varphi)=\exp(ia\varphi^p)$ are provided, showing that, in these cases, one spiral loop is always formed. The coefficients a are chosen so that the TVSs coincide, with the GSPPs with the same TVSs forming substantially different curves.

1. Function $g(\varphi)=\varphi^2$

In this case, the TVS is equal to 2π. The local TC is defined as $n_c=2\varphi$, and the nth sector is defined by inequality $n/2\leqslant\varphi\leqslant(n+1)/2$; that is, all sectors have the same angular size and same area. The sector boundaries and corresponding values $\gamma'_{1,n}$ (taken from [22]) are given in Table I. Since the values $\gamma'_{1,n}$ do not depend on the type of function $g(\varphi)$, only on the index, they are only presented in this example.

2. Function $g(\varphi)=\varphi^3/(2\pi)$

For a GSPP with $g(\varphi)=a\varphi^3$, TVS is equal to $a(2\pi)^2$. In order to calculate the TVS similar to the previous example, it is necessary to choose the coefficient a equal to $(2\pi)^{-1}$; then, the TVS is equal to 2π. The local TC is defined as $n_c=$

TABLE I. Sector boundaries and corresponding envelope sizes for the function $g(\varphi) = \varphi^2$.

n	0	1	2	3	4	5	6
Sector boundaries, rad	0.5	1	1.5	2	2.5	3	3.5
$\gamma'_{1,n}$	1.84	3.05	4.20	5.32	6.41	7.50	8.58
n	7	8	9	10	11	12	
Sector boundaries, rad	4	4.5	5	5.5	6	2π	
$\gamma'_{1,n}$	9.65	10.7	11.75	12.82	13.85	14.90	

$3\varphi^2/2\pi \approx 0.477\varphi^2$ and the nth sector is defined by the inequality $\sqrt{\frac{2\pi n}{3}} \leqslant \varphi \leqslant \sqrt{\frac{2\pi(n+1)}{3}}$ (approximately $1.447\sqrt{n} \leqslant \varphi \leqslant 1.447\sqrt{n+1}$). Thus, in this example, the size of the sectors decreases with an increase in their numbers. The sector boundaries are given in Table II.

3. Function $g(\varphi) = \sqrt{2\pi}\varphi^{3/2}$

In this case, the coefficient $a = (2\pi)^{1/2}$ was also chosen to obtain the TVS equal to 2π as in the previous examples. The local TC is defined as $n_c = \sqrt{2\pi}\frac{3}{2}\varphi^{1/2} \approx 3.76\varphi^{1/2}$, and the nth sector is defined by the inequality $\frac{2n^2}{9\pi} \leqslant \varphi \leqslant \frac{2(n+1)^2}{9\pi}$ [approximately $0.0707n^2 \leqslant \varphi \leqslant 0.0707(n+1)^2$]. In this example, the size of the sectors increases with an increase in their numbers. The sector boundaries are given in Table III.

An analysis of the calculated results of the presented three examples shows that the sizes of sectors decrease with increasing number if the derivative $g'(\varphi)$ is convex downward ($p > 2$ and, as we will see below, $0 < p < 1$), and increase if the derivative $g'(\varphi)$ is convex upward ($1 < p < 2$). From the above reasoning, it follows that it is possible to choose such a smooth function $g(\varphi)$, so that the curve formed in the focal plane has points with an arbitrarily large radius. For this, it is enough that the derivative is not limited in magnitude, as illustrated by the following example.

4. Function $g(\varphi) = (2\pi)^{3/2}\varphi^{1/2}$

In this case, the coefficient $a = (2\pi)^{3/2}$ was also chosen to obtain the TVS equal to 2π. The local TC is defined as $n_c = (2\pi)^{3/2}\frac{1}{2}\varphi^{-1/2} \approx 7.875\varphi^{-1/2}$ and the nth sector is defined by inequality $\frac{2\pi^3}{(n+1)^2} \leqslant \varphi \leqslant \frac{2\pi^3}{n^2}$ (approximately $\frac{62}{(n+1)^2} \leqslant \varphi \leqslant \frac{62}{n^2}$). The derivative decreases, so it is convenient to number the sectors from the end (from an angle of 360°), and the minimum number may not be zero. Another difference from the previous examples is that, due to the unboundedness of the derivative, there is no maximum number. Obviously, the sectors are contracting unlimitedly. The sector boundaries and envelope radii are shown in Table IV.

TABLE II. Sector boundaries for the function $g(\varphi) = \varphi^3/(2\pi)$.

n	0	1	2	3	4	5	6
Sector boundaries, rad	1.45	2.05	2.51	2.89	3.24	3.54	3.83
n	7		15	16	17	18	
Sector boundaries, rad	4.09		5.79	5.97	6.14	2π	

TABLE III. Sector boundaries for the function $g(\varphi) = \sqrt{2\pi}\varphi^{3/2}$.

n	0	1	2	3	4
Sector boundaries, rad	0.07	0.28	0.64	1.13	1.77
n	5	6	7	8	9
Sector boundaries, rad	2.55	3.47	4.53	5.73	2π

III. EXPERIMENTAL RESULTS

A. Light field distributions generated by GSPPs in the far-field region

Let us demonstrate some features of the light fields generated by GSPPs on the example of the GSPP with the transmission function of $\exp(im\varphi^s)$. Figure 2(a) shows the experimental setup for the investigation of the properties of light field distributions generated by GSPPs in the far-field region. To experimentally realize the transmission function of the nonlinear SPP, we used a spatial light modulator (SLM) HOLOEYE LC2012 (pixel resolution of 1024×768 and pixel size of 36 μm). In the experiments, a linearly polarized Gaussian laser beam from a solid-state laser ($\lambda = 532$ nm; $w_0 = 2$ mm) was extended and collimated with a combination of a microobjective MO (8 ×), pinhole PH with an aperture size of 40 μm, and a lens L1 with the focal length of 500 mm. Afterwards, the laser beam was passed through the SLM, and the modulated laser beam was focused with the help of a lens L2 with the focal length of 350 mm. To obtain the phase distribution of the experimentally generated laser fields, the Mach-Zehnder interferometer consisting of two beamsplitters BS1, BS2 and two mirrors M1 and M2 was used to capture the fringe patterns between the generated laser beam and the reference Gaussian beam with a flat wave front. The generated intensity distributions and fringe patterns were recorded by a video camera *Cam* (TOUPCAM UHCCD00800KPA; 1600×1200 pixels, with a pixel size of 3.34 μm). To reconstruct the phase distributions from the experimentally obtained fringe patterns, an approach with a parallel interference between the generated laser beam and a reference beam was applied [23]. This approach implies capturing two fringe patterns for each phase profile measurement, one of which is obtained with the additional $\pi/2$ phase shift between the paths of interferometer that was introduced with the help of a quarter wave plate QP [see Fig. 2(b)]. A neutral density filter F was used to equalize the intensities of the

TABLE IV. Sector boundaries for the function $g(\varphi) = (2\pi)^{3/2}\varphi^{1/2}$.

n	3	4	5	6
Sector boundaries, rad	3.88	2.48	1.72	1.27
n	10		19	20
Sector boundaries, rad	0.51		0.16	0.14

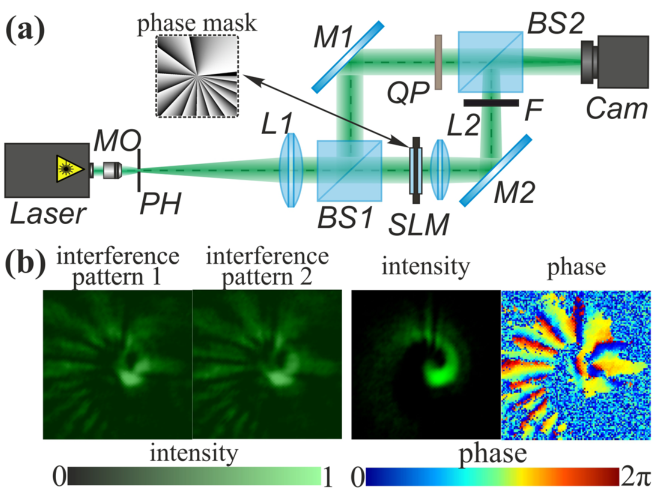

FIG. 2. (a) Experimental setup for the investigation of the properties of light field distributions generated by GSPPs. (b) Examples of the captured interference patterns and intensity distribution used for phase map reconstruction in the case of the GSPP with the transmission function of $\exp(im\varphi^s)$, $s = 2$, and $m = -2$.

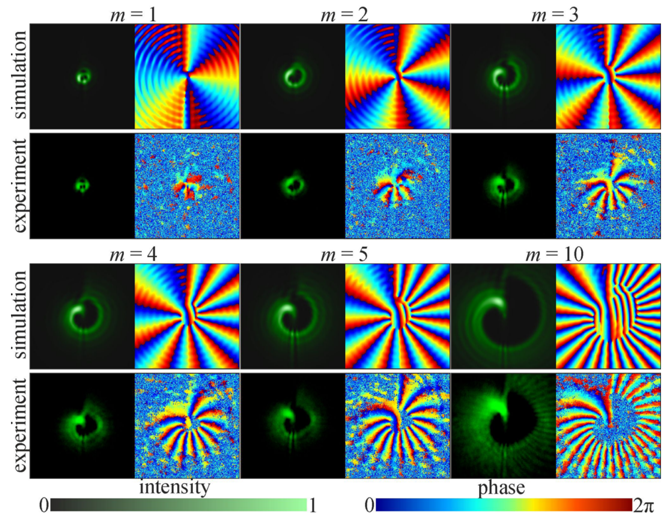

FIG. 4. Numerically and experimentally obtained intensity and phase distributions generated by GSPPs with the transmission function of $\exp(im\varphi^s)$, fixed power value $s = 1.5$, and different m.

object and the reference beams. The experimentally obtained results were in good agreement with the numerically obtained results, generating nonring intensity distributions with spiral wave fronts in the case of nonlinear SPPs with $s \neq 1$, and the dimensions of the generated distributions increase with an increase in s.

Figure 3 shows the numerically calculated and experimentally obtained intensity and phase distributions for a nonlinear SPP with a complex function of $\exp(im\varphi^s)$ for various values of the power value s. The fast Fourier transformation was used for the calculation of the far-field light distributions.

Figure 4 shows the light field distributions generated in the case of nonlinear SPPs with a fixed value of power value s and various values of m. The situation analogous to the conventional SPPs occurs in this case: an increase in the value of m leads to an increase in the dimensions of the generated light distributions, which can also be explained by the fact that the radii of two envelope circles limiting the generated light curve increase with an increase in the value of m.

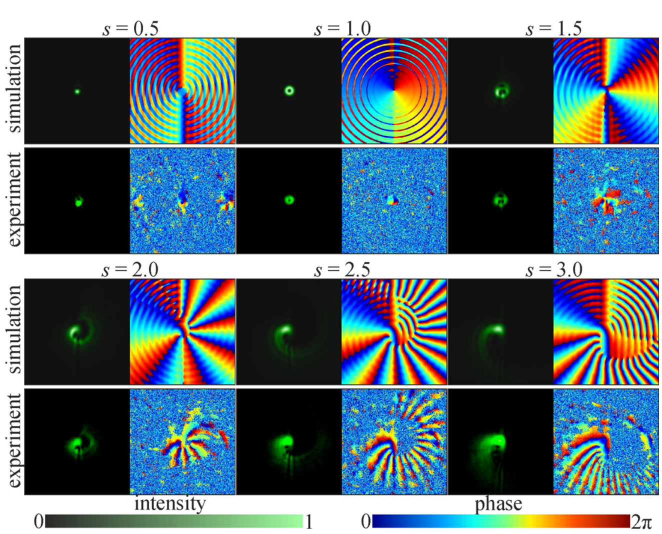

FIG. 3. Numerically and experimentally obtained intensity and phase distributions generated by GSPPs with the transmission function of $\exp(im\varphi^s)$, fixed $m = 1$, and different power values s.

B. Energy flow of the light fields generated by GSPPs in the far-field region

It is well known that, in the case of the conventional SPP, the sign of the TC defines the direction of the phase gradient of the generated spiral wave front [24]. The same situation occurs in the case of the GSPP; however, the generated intensity distribution also changes, with the light spiral mirrored relative to the origin [see Fig. 5(a)]. For negative values of m, the directions of the intensity gradient and phase gradient coincide and, for positive values of m, the directions of these gradients are opposite. The calculated energy flows for the cases of positive and negative signs of the TC are shown in Fig. 5(b). The energy flows were computed as the transverse components of the Poynting vector using the expression $J(x, y) = I(x, y)\nabla\varphi(x, y)$, where $I(x, y)$ is the intensity and $\nabla\varphi(x, y)$ is the transverse phase gradient [25].

The energy flows have a spiral-shaped form in both cases of different sign of $m = \pm 2$, in contrast to the annular energy flow in the case of the light rings generated by conventional SPPs. Such energy flow that depends on the sign of the m is useful for laser material processing, especially in the case of processing azopolymers because, in this case, the shape of the laser-fabricated nano- and microstructures is sensitive, not only to the intensity distribution, but also to the complex amplitude of the illuminating laser beam.

C. Angle-dependent distortion resistance properties of the light fields generated by GSPPs

Another feature of GSPP that should be investigated is the stability of the light distribution generated by the elements to distortions. The root-mean-square error (RMSE) σ for the

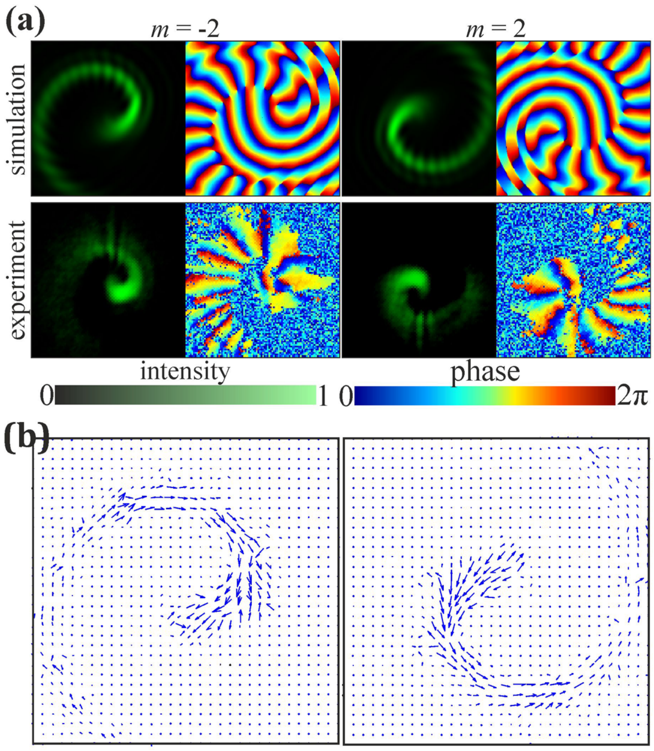

FIG. 5. (a) Numerically and experimentally obtained intensity and phase distributions generated by GSPPs with the transmission function of $\exp(im\varphi^s)$, fixed power value $s = 2$, and $m = \pm 2$. (b) Computed energy flow of the generated far-field light spirals.

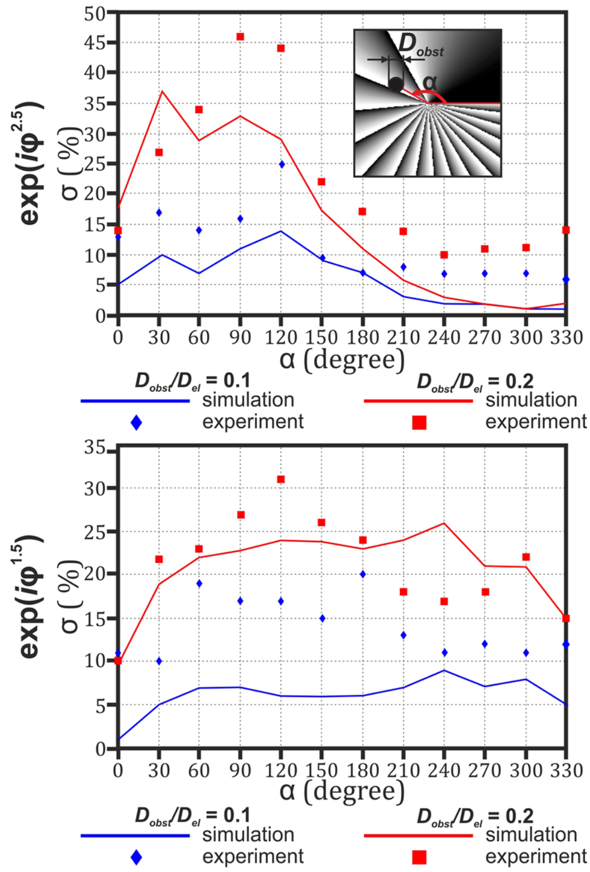

FIG. 6. RMSE σ of the spiral-shaped intensity distributions generated by the GSPP with two different transmission functions $\exp(i\varphi^{1.5})$ and $\exp(i\varphi^{2.5})$ versus angular coordinates of the opaque obstacles with different diameters D_{obst}. Inset shows the distorted transmission function used in the experiments and the parameters used for investigations.

generated intensity distributions is defined as

$$\sigma = \sqrt{\frac{\sum (I_{\text{dist}} - I_{\text{ideal}})^2}{\sum I_{\text{ideal}}^2}}, \tag{18}$$

where where I_{ideal} and I_{dist} are the experimentally obtained intensity distributions generated by nondistorted and distorted elements, respectively. In the case of the conventional SPP, there is practically no difference in RMSE values if the distortion is located on the same radius at different angular coordinates. However, the unique structure of the GSPP leads to different RMSE values. The results obtained in the case of the circle opaque obstacles with different diameters are presented in Fig. 6. The RMSE values vary with the variation of the angle α that defines the angular position of the obstacle in both obstacles. In addition, the structure of the variation of the RMSE value is similar in both cases and for two different transmission functions of the SPPs, $\exp(i\varphi^{1.5})$ and $\exp(i\varphi^{2.5})$. The minimal values are for angles from 300° to 360 (0)°, the sectors where the phase gradients have maximal values; the angular sector with these angles is limited to two envelope circles with larger radii. In addition, the intensity of the part of the light spiral generated by this angular sector is lower in comparison with other parts. Thus the distortion of this angular sector leads to an insignificant distortion of the generated light spiral. In addition, increasing the phase gradient results increases the rate of phase change in the propagation direction, which also accelerates the light field reconstruction process [26]. Even though the simulation reproduces the behavior of experimental results, there is some discrepancy between the experimentally and numerically obtained values of the RMSE. This can be explained by the additional distortions of the experimentally generated light field due to aberrations in the experimental setup. In addition, the pixilated structure and relatively large (36 μm) pixel size of the SLM realized the designed phase masks and the fluctuation of the profile of the used Gaussian beam from the ideal Gaussian beam led to some distortions of the experimentally generated light fields.

D. Angular harmonics spectra and OAM density of the light fields generated by GSPPs

It is well known that the angular harmonics spectrum of the light field generated by a conventional SPP contains only one term corresponding to the TC of the element and there is almost no dependence of the distortion of the spectra on the angular coordinate of the obstacle (see Fig. 7). In the case of GSPP, from the analysis of the structure of the angular harmonics spectra of the generated light fields shown in Fig. 7, two main conclusions can be obtained: (1) the number of angular harmonics in the spectrum increases with an increase in the power value s [in the general case, the increase in the number of generated angular harmonics is

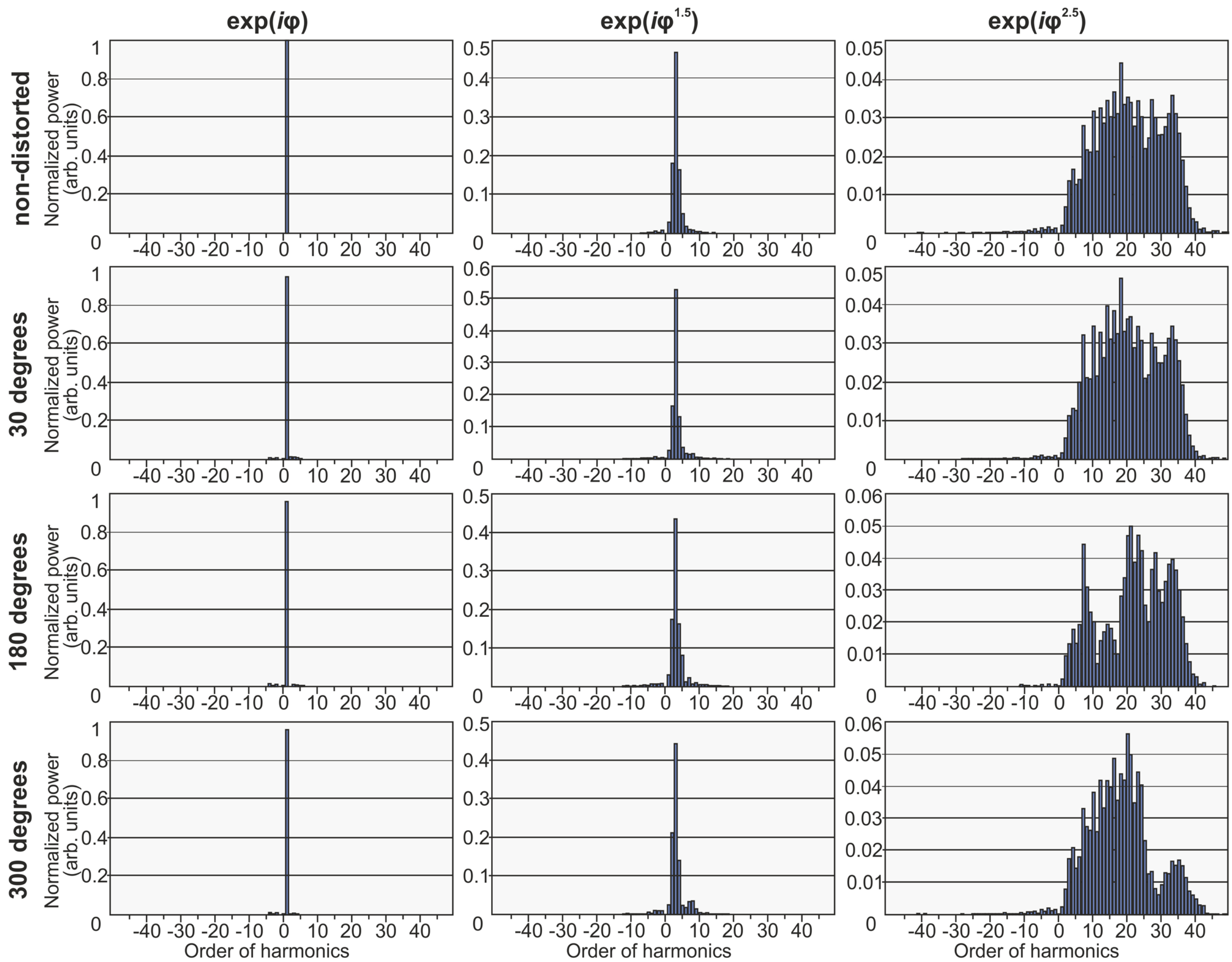

FIG. 7. Angular harmonics spectra of the light fields generated in the case of a nondistorted and distorted GSPP: $D_{\mathrm{obst}}/D_{\mathrm{el}} = 0.2$.

associated with the growth rate of the function $g(\varphi)$]; (2) for the GSPP with increasing power value *s*, the structure of the angular harmonics spectra strongly depends on the angular coordinate of the opaque obstacle. The first conclusion can be explained by the fact mentioned above—that the increase in the growth rate of the function $g(\varphi)$ leads to the increase in the number of different sectors n in the structure of the envelope of the generated light spirals (see Tables I–III). As mentioned previously, each sector corresponds to the SPP with its own local TC, so the generated vortex light field is a superposition of different angular harmonics. The second conclusion is also explained by the same fact—that the increase in the number of sectors leads to the decrease in their sizes. The distortion of the individual angular harmonics caused by the obstacle depends on the size of the sector—the smaller the size of the sector, the more distortion of the corresponding angular harmonic generated by this sector.

It is obvious that angular-dependent distortion of the intensity distribution and angular harmonics spectra of the generated vortex light fields leads to the distortion of the OAM of the field. The OAM density of the complex field $E(x, y)$ defined in the Cartesian coordinates (x, y) can be calculated as follows [27]:

$$M(x, y) = \mathrm{Im}\left\{E(x, y)^* \left[x\frac{\partial E(x, y)}{\partial y} - y\frac{\partial E(x, y)}{\partial x}\right]\right\}. \quad (19)$$

From Fig. 8, the OAM density of the light field generated by the GSPPs is nonuniform in contrast to the light fields generated by conventional SPPs [4]: the central part of the generated spiral-shaped distribution has the maximal value of the OAM density and the generated light spiral has a gradient of OAM density similar to the energy flow. The normalized OAM calculated by Eq. (6) for the light fields generated by these two investigated nondistorted elements is approximately 2.51 and 15.75, respectively. Also, the OAM of the generated spiral-shaped light field depends on the angular coordinates of the obstacle. In addition, similar to the angular harmonics spectra, the increase in the growth rate of the function $g(\varphi)$ leads to stronger fluctuations of the total OAM [2% and 7% in the case of the GSPP with the transmission function of $\exp(i\varphi^{1.5})$; 4% and 11% in the case of the GSPP with the transmission function of $\exp(i\varphi^{2.5})$ for two different diameters of the obstacle, $D_{\mathrm{obst}}/D_{\mathrm{el}} = 0.1$ and $D_{\mathrm{obst}}/D_{\mathrm{el}} = 0.2$]. As mentioned above for the measurements of the RMSE values,

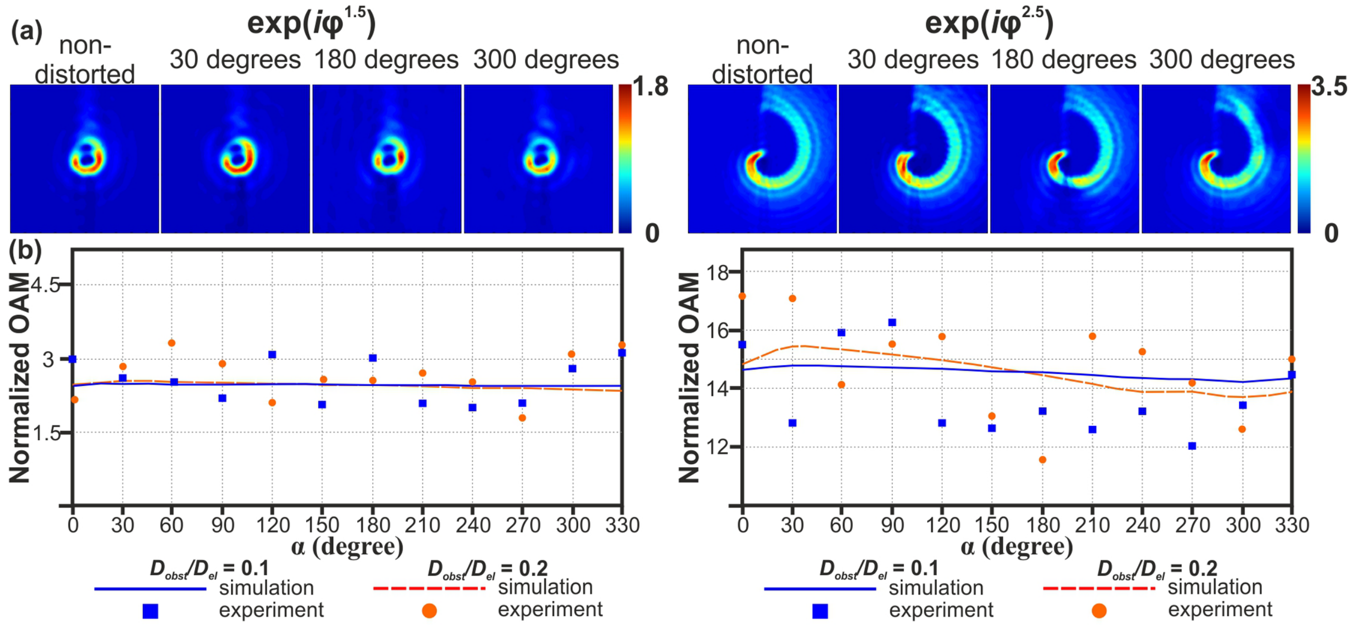

FIG. 8. (a) OAM density of the light field generated in the case of a nondistorted and distorted nonlinear SPP: $D_{\mathrm{obst}}/D_{\mathrm{el}} = 0.2$. (b) Normalized OAM of the generated light field versus angular coordinate of the opaque obstacles with different diameters D_{obst}.

there are some discrepancies between the experimentally and numerically obtained values of the normalized OAM due to aberrations in the experimental setup. However, the general structure of the dependence obtained in the experiment and simulation coincides; that is, larger obstacles lead to the greater distortions of the normalized OAM.

IV. CONCLUSIONS

We theoretically and experimentally investigated generalized spiral phase plates with a transmission function of $\exp[ig(\varphi)]$ defined by the function $g(\varphi)$, showing that the nonlinear spiral phase plate can be used for the generation of nonring (including spiral-shaped) laser beams with a helical wave front. The total vortex strength of the proposed generalized spiral phase plates, a value analogous to the topological charge of a conventional spiral phase plate, is defined as $[g(2\pi) - g(0)]/2\pi$ and equal to the normalized orbital angular momentum of the generated light field.

The distortion resistance properties of the proposed element show angular dependence: different values of root-mean-square error are obtained for different angular positions of an opaque obstacle. In addition, the angular harmonics spectra of the generated vortex light fields and their total orbital angular momentum strongly depend on the growth rate of the function $g(\varphi)$, with the orbital angular momentum density of the generated light fields being nonuniform. Despite the fact that we only studied the case of a plate with a power function $\exp(im\varphi^s)$ in the experiments, the conclusions obtained in this work can be applied to light fields generated by an arbitrary generalized spiral phase plate $\exp[ig(\varphi)]$ with an arbitrary function $g(\varphi)$. The phase structure of the transmission functions of generalized spiral phase plates are very similar in all cases of the function $g(\varphi)$ – it is sectors with different angular sizes. The experimentally and numerically obtained results are in good agreement. We believe that the proposed diffractive optical elements are useful, primarily for optical manipulation application for realization of optical rotation and guiding of the nano- and microparticles, as well as for creation of micropumps and microrotors [28]. In addition, such spiral-shaped laser beams can be used for realization of laser fabrication of chiral nano- and microelements for 2D and 3D metasurfaces [29].

ACKNOWLEDGMENTS

This work was financially supported by Russian Foundation for Basic Research (RFBR) (Grant No. 20-37-70025) and RF Ministry of Science and Higher Education (Grant No. 007-GZ/Ch3363/26).

[1] S. N. Khonina, V. V. Kotlyar, M. V. Shinkaryev, V. A. Soifer, and G. V. Uspleniev, The phase rotor filter, J. Mod. Opt. **39**, 1147 (1992).

[2] T. V. Higgins, Spiral waveplate design produces radially polarized laser light, Laser Focus World **28**, 18 (1992).

[3] J. E. Curtis and D. G. Grier, Structure of Optical Vortices, Phys. Rev. Lett. **90**, 133901 (2003).

[4] L. Allen, M. W. Beijersbergen, R. J. C. Spreeuw, and J. P. Woerdman, Orbital angular momentum of light and the transformation of Laguerre-Gaussian laser modes, Phys. Rev. A **45**, 8185 (1992).

[5] N. B. Simpson, K. Dholakia, L. Allen, and M. J. Padgett, Mechanical equivalence of spin and orbital angular momentum of light: an optical spanner, Opt. Lett. **22**, 52 (1997).

[6] A. E. Willner, H. Huang, Y. Yan, Y. Ren, N. Ahmed, G. Xie, C. Bao, L. Li, Y. Cao, Z. Zhao, J. Wang, M. P. J. Lavery, M. Tur, S. Ramachandran, A. F. Molisch, N. Ashrafi, and S. Ashrafi, Optical communications using orbital angular momentum beams, Adv. Opt. Photon. **7**, 66 (2015).
[7] M. Ritsch-Marte, Orbital angular momentum light in microscopy, Philos Trans. A: Math. Phys. Eng. Sci. **375**, 20150437 (2017).
[8] K. Toyoda, F. Takahashi, S. Takizawa, Y. Tokizane, K. Miyamoto, R. Morita, and T. Omatsu, Transfer of Light Helicity to Nanostructures, Phys. Rev. Lett. **110**, 143603 (2013).
[9] S. Syubaev, A. Zhizhchenko, A. Kuchmizhak, A. Porfirev, E. Pustovalov, O. Vitrik, Yu. Kulchin, S. Khonina, and S. Kudryashov, Direct laser printing of chiral plasmonic nanojets by vortex beams, Opt. Express **25**, 10214 (2017).
[10] S. Syubaev, A. Zhizhchenko, O. Vitrik, A. Porfirev, S. Fomchenkov, S. Khonina, S. Kudryashov, and A. Kuchmizhak, Chirality of laser-printed plasmonic nanoneedles tunable by tailoring spiral-shape pulses, Appl. Surf. Sci. **470**, 526 (2019).
[11] S. Cheng, L. Wu, and S. Tao, Annular beam with segmented phase gradients, AIP Adv. **6**, 085322 (2016).
[12] S. Cheng, T. Xia, M. Liu, Y. Xu, S. Xu, S. Gao, G. Zhang, S. Tao, and W. Yang, Ring-broken optical vortices with an adjustable opening, Results Phys. **15**, 102689 (2019).
[13] P. Li, S. Liu, T. Peng, G. Xie, X. Gan, and J. Zhao, Spiral autofocusing Airy beams carrying power-exponent-phase vortices, Opt. Express **22**, 7598 (2014).
[14] G. Lao, Z. Zhang, and D. Zhao, Propagation of the power-exponent-phase vortex beam in paraxial ABCD system, Opt. Express **24**, 18082 (2016).
[15] J. Wang, X. Qiu, Q. Lu, W. Zhang, and L. Chen, OAM content and propagation dynamics of integer-order Gamma vortices, Opt. Commun. **459**, 125053 (2020).
[16] A. J. Jesus-Silva, E. J. S. Fonseca, and J. M. Hickmann, Study of the birth of a vortex at Fraunhofer zone, Opt. Lett. **37**, 4552 (2012).
[17] M. Luo and Z. Wang, Fractional vortex ultrashort pulsed beams with modulating vortex strength, Opt. Express **27**, 36259 (2019).
[18] M. V. Berry, Optical vortices evolving from helicoidal integer and fractional phase steps, J. Opt. A: Pure Appl. Opt. **6**, 259 (2004).
[19] S. N. Khonina, V. V. Kotlyar, V. A. Soifer, P. Paakkonen, J. Simonen, and J. Turunen, An analysis of the angular momentum of a light field in terms of angular harmonics, J. Mod. Opt. **48**, 1543 (2001).
[20] N. Zhang, J. A. Davis, I. Moreno, J. Lin, K.-J. Moh, D. M. Cottrell, and X. Yuan, Analysis of fractional vortex beams using a vortex grating spectrum analyzer, Appl. Opt. **49**, 2456 (2010).
[21] V. V. Kotlyar, S. N. Khonina, A. A. Kovalev, V. A. Soifer, H. Elfstrom, and J. Turunen, Diffraction of a plane, finite-radius wave by a spiral phase plate, Opt. Lett. **31**, 1597 (2006).
[22] M. Abramowitz and I. A. Stegun, *Handbook of Mathematical Functions* (Courier Dover Publications, Mineola, NY, 1972).
[23] S. Paul, V. S. Lyubopytov, M. F. Schumann, J. Cesar, A. Chipouline, Ma. Wegener, and F. Küppers, Wavelength-selective orbital-angular-momentum beam generation using MEMS tunable Fabry-Perot filter, Opt. Lett. **41**, 3249 (2016).
[24] A. M. Yao and M. J. Padgett, Orbital angular momentum: origins, behavior and applications, Adv. Opt. Photon. **3**, 161 (2011).
[25] B. K. Singh, M. Bahl, D. S. Mehta, and P. Senthilkumaran, Study of internal energy flows in dipole vortex beams by knife edge test, Opt. Commun. **293**, 15 (2013).
[26] F. Saadati-Sharafeh, A. Borhanifar, A. P. Porfirev, P. Amiri, E. A. Akhlaghi, S. N. Khonina, and Y. Azizian-Kalandaragh, The superposition of the Bessel and mirrored Bessel beams and investigation of their self-healing characteristic, Optik **199**, 164057 (2019).
[27] A. M. Caravaca Aguirre and T. Alieva, Orbital angular momentum density of beam given as a superposition of Hermite-Laguerre-Gauss functions, Prog. Electromagn. Res. **2011**, 250 (2011).
[28] U. G. Būtaitė, G. M. Gibson, Y.-L. D. Ho, M. Taverne, J. M. Taylor, and D. B. Phillips, Indirect optical trapping using light driven micro-rotors for reconfigurable hydrodynamic manipulation, Nat. Commun. **10**, 1215 (2019).
[29] J. Ni, C. Wang, C. Zhang, Y. Hu, L. Yang, Z. Lao, B. Xu, J. Li, D. Wu, and J. Chu, Three-dimensional chiral microstructures fabricated by structured optical vortices in isotropic material, Light Sci. Appl. **6**, e17011 (2017).